Large Sign Reversal of Tunneling Magnetoresistance in an Epitaxial Fe/MgAlO x /Fe 4 N Magnetic Tunnel Junction

Tianyi Ma, Yu Zhu, Pambiang Abel Dainone, Tongxin Chen, Xavier Devaux, Caihua Wan, Sylvie Migot, Gwladys Lengaigne, Michel Vergnat, Yu Yan, et al.

Large sign-reversal of tunneling magnetoresistance in epitaxial Fe/$MgAlO_x$/Fe_4N magnetic tunnel junction

Tianyi Ma,[1,2] Yu Zhu,[3] Pambiang Abel Dainone,[2] Tongxin Chen,[2] Xavier Devaux,[2] Caihua Wan,[1] Sylvie Migot,[2] Gwladys Lengaigne,[2] Michel Vergnat,[2] Yu Yan,[3] Xiufeng Han,[1‡] Yuan Lu[2*]

[1]*Beijing National Laboratory for Condensed Matter Physics, Institute of Physics, University of Chinese Academy of Sciences, Chinese Academy of Sciences, Beijing 100190, China.*
[2]*Institut Jean Lamour, CNRS-Université de Lorraine, UMR 7198, 54011 Nancy, France*
[3]*Key Laboratory of Physics and Technology for Advanced Batteries, Department of Physics, Jilin University, Changchun 130012, China*

Corresponding authors: * *yuan.lu@univ-lorraine.fr*; ‡ *xfhan@iphy.ac.cn*

Abstract

A sign-reversible tunneling magnetoresistance (TMR) bestows an extra control freedom to design TMR-based spintronic devices for developing spin logic applications. Here, we demonstrate a large sign-reversal of TMR in an epitaxial Fe/$MgAlO_x$/Fe_4N magnetic tunnel junction (MTJ) controlled by the bias voltage. At room temperature (RT), the TMR is measured as large as −26.7% (−38% under optimistic definition) at V=+0.45V and it changes the sign to be +3.2% at V=−0.6V. The TMR sign-reversal effect is doubled compared to the Fe/MgO/Fe_4N MTJs, which is attributed to the better lattice mismatch between Fe_4N and $MgAlO_x$ as well as less N diffusion inside the tunneling barrier. First principle calculations reveal that the change of TMR sign originates from different symmetry-dependent tunneling channels between Fe and Fe_4N electrodes under opposite bias voltages. The Fe/$MgAlO_x$/Fe_4N MTJ with voltage-controllable TMR signs and relatively large TMR ratios at RT will promote the development of versatile and reprogrammable spintronic logic applications.

Keywords: magnetic tunnel junction, inverse magnetoresistance, symmetry-dependent tunneling, magnetic random-access memories, spin logic

Introduction

The tunnel magnetoresistance (TMR) effect in magnetic tunnel junctions (MTJ) is one of cornerstones of spintronics[1–5] that has resulted in broad applications such as magnetic random-access memories (MRAM), magnetic sensors, spin logics and neuromorphic computing devices.[6–11] Pioneering works has shown that a single MTJ can work as a multi-functional logic gate by properly configurating magnetizations of both free and reference magnetic layers.[12] However, switching the reference layer consumes redundant energy and lowers the thermal stability of devices. The multifunctional logic gate can also be realized in magnetic heterostructures where the perpendicular magnetization of the free layer is switched by the spin-orbit torque and controlled by an effective in-plane field.[13,14] However, reading out signals from these logic gates relies on the anomalous Hall effect which is less sensitive than the TMR effect. Recently, a novel proposal[15] emerges to build such spin logic devices by utilizing MTJs with voltage-controllable and sign-reversible TMR effect. Combining two of these MTJs and one current comparator, a real-time reprogrammable logic gate can be built, in which all four functions: AND, OR, NAND and NOR are realized and switchable by initializing only the free-layer magnetization of the two MTJs.[15] To realize such spin logic function, a MTJ system with large sign-reversible TMR at room temperature (RT) is indispensable.

The sign-reversible TMR phenomena have been reported in several systems due to various mechanisms. For instance, the TMR ratio of the NiFe/composite Ta_2O_5/Al_2O_3/NiFe MTJs varies from +1% to -4% with different bias at RT.[16] Its sign inversion is resulted from different densities of states (DOS) at two electrode/barrier interfaces. In Ni/NiO/Co nanowires, the TMR ratio can be inverted by voltage due to the matching of the energy of localized states in NiO, which is sensitive to the quality of the barrier, with the Fermi energy of ferromagnetic electrodes.[17] In $La_{0.67}Sr_{0.33}MnO_3$(LSMO)/$SrTiO_3$(STO)/SrO/Co MTJs, their TMR ratio varies from +8% to −15%

with applied voltage at 85 K.[18] The sign of TMR ratio is found to be very sensitive to the interface spin polarization at $SrTiO_3$/Co interface with one atomic insertion layer of TiO_2 or SrO as well as the oxygen content in the barrier. In addition, MTJs with Fe_3O_4 electrode and MgO barrier also show a reversal TMR sign effect. Depending on the materials used for the second electrode (Co[19], CoFeB[20] and Fe[21]), the maximum negative TMR have been demonstrated to be -8.5%, -12% and -9.6% at RT, respectively. Recently, the multiferroic tunnel junctions (MFTJs) combining the ferroelectric tunnel barrier with ferromagnetic electrodes attract intensive interests. In such systems, TMR and tunneling electroresistance (TER) coexist and the sign of TMR can be modulated by changing the ferroelectric polarization of ferroelectric tunnel barrier. In Co/$PbZr_{0.2}Ti_{0.8}O_3$(PZT)/LSMO MFTJ, the TMR ratio varies from +4% to -3% with a ±3 V polarizing voltage pulse at 50 K.[22] In LSMO/ Polyvinylidene fluoride(PVDF) or P(VDF-TrFE)/Co MFTJs, the TMR ratio varies from +8.3% to -12.5% with a ±1.5 V polarizing voltage pulse at 10 K.[23,24] Note that LSMO is usually chosen as the ferromagnetic electrode to obtain high spin polarization and well-defined ferromagnetic/ferroelectric interfaces. However, the low Curie temperature of LSMO hampers its room-temperature applications. Another issue for the MFTJ is that the TMR will be suppressed if the ferroelectric barrier is too thick, since the transport mechanisms are different from direct tunnelling.[25] Thus, a trade-off relating to an optimized thickness of the ferroelectric barrier must be taken into account to keep both effects (TMR and TER) sizable.[24]

Although many systems have been demonstrated for the sign-reversal TMR effect, the amplitude of TMR is small and operation temperature is low. Recently, Fe_4N has been demonstrated to have high negative spin-polarization,[26–28] unique magnetic structure and low critical switching current density.[29,30] These merits co-make Fe_4N MTJs suitable for spintronic applications and also a potential candidate to achieve the sign-reversible TMR effect. In this work, we have epitaxially grown

Fe/$MgAlO_x$/Fe_4N MTJ by molecular beam epitaxy (MBE). We have observed a voltage-dependent TMR ratio which can be modulated from +3.2% to −26.7% at RT, showing a superior performance than previous reported results. From first principle calculations, the sign-reversible TMR phenomenon is found to be relevant to the symmetry-dependent tunneling process between Fe and Fe_4N electrodes. The voltage-controllable TMR signs and relatively large TMR ratios, especially at RT will contribute to develop the real-time reprogrammable spin logic gates for different spintronic applications.

Results and discussions

Structure and chemistry study by STEM combined with EELS

The magnetic tunnel junction stack consisting of MgO(001) substrate||MgO(10 nm)/Fe(45 nm)/$MgAlO_x$(0.6 nm)/Fe(7 nm)/$MgAlO_x$(2.5 nm)/Fe_4N(3 nm)/Co(20 nm)/Au(10 nm) was grown in a MBE system. The epitaxial growth and annealing process were controlled by high-energy electron diffraction (RHEED). The detailed growth condition can be found in **Methods** and **Supporting Information (SI) Notes 1** and **2**. For comparison, another sample with MgO tunneling barrier was grown consisting of stack structures: MgO(001) substrate||MgO(10 nm)/Fe(45 nm)/MgO(2.5 nm)/Fe_4N(3 nm)/Co(20 nm)/Au(10 nm). High-resolution scanning transmission electron microscope (HR-STEM) characterizations were performed to verify the structure of the MTJs. **Figs. 1(a,b)** shows the high-angle annular dark-field (HAADF) images for $MgAlO_x$ MTJ in a large and magnified scale, respectively. In **Fig. 1(a)**, one can observe sharp interfaces between $MgAlO_x$ (in black contrast) and Fe or Fe_4N layers (in grey contrast). The $MgAlO_x$ barrier layer appears quite flat and continuous, indicating a high quality of MTJ structure without any pinholes. The magnified image in **Fig. 1(b)** further proves the epitaxial growth characters with well-aligned atomic arrays between Fe, $MgAlO_x$

and Fe_4N layers. Bulk Fe_4N has a cubic antiperovskite structure, and the lattice constant is reported to be 3.795 Å in experiment.[31] Despite the large lattice mismatch of 6.5% between Fe_4N and $MgAl_2O_4$ (lattice constant 4.212Å[31]), the epitaxial crystalline relationship can be determined to be Fe[110]//$MgAlO_x$[100]//Fe_4N[100] combined with RHEED analysis (see **SI Note 1** and **3**). However, Co on Fe_4N exhibits large disorientated polycrystalline features. For MTJ with MgO barrier, one can also observe an epitaxial growth of Fe_4N on MgO (see **SI Note 2** and **4**), however the intensity of RHEED appears weaker and more crystalline deformation can be found in the Fe_4N layer (see **SI Figs. S2** and **S3(b)**), which could be attributed to the larger lattice mismatch (11%) between Fe_4N and MgO (see more discussion in **SI Note 3**).

To characterize the interfacial chemistry structure of MTJ multilayers, the element distribution analyses were performed by STEM combined with spatially resolved electron energy loss spectroscopy (EELS) characterizations. **Figs. 1(d-i)** show semi-quantitative chemical maps drawn by processing the EELS spectrum images. A sharp chemical interface is found between Fe and $MgAlO_x$ layers. However, from the element mapping of N (**Fig. 1(d)**), a partial N diffusion towards $MgAlO_x$ barrier can be detected at $MgAlO_x$/Fe_4N interface. This N diffusion can be also clearly evidenced by a larger peak width (red line) compared to the Fe peak (blue line) in the element intensity profiles, as shown in **Fig. 1(c)**. Here, a background signal of Al can be found, which is mainly due to the artefact during the signal processing of EELS peaks. For MTJs with MgO barrier, the situation of N diffusion is more pronounced. In **SI Figs. S3(c,d)** (see **SI Note 4**), one can observe that N can penetrate MgO barrier and even reach the bottom Fe/MgO interface. The diffusion of N could be attributed to the oxygen vacancy in the MgO and $MgAlO_x$ barriers. Since the bond energy for Fe-N (350 kJ/mol)< Mg-O (380 kJ/mol) < Mg-N (400 kJ/mol) < Al-O (510 kJ/mol) < Al-N (650 kJ/mol),[32] ionic N species tend to diffuse into MgO or $MgAlO_x$ barrier to occupy oxygen vacancy position during Fe_4N growth.

For $MgAlO_x$ barrier, the formation of Al-N bonds can help to stop further diffusion of N inside the barrier. Nevertheless, the N diffusion can easily penetrate MgO barrier because of the low bond energy of Mg-N, which is comparable to Fe-N bond, thus resulting in an accumulation of N at the bottom Fe/MgO interface. The element concentration in the $MgAlO_x$ barrier is found to be Mg:Al:O=1:0.2:1.3, far from the stoichiometric condition for spinel $MgAl_2O_4$ structure (Mg:Al:O=1:2:4), indicating possible Al and O vacancies in our $MgAlO_x$ barrier. In addition, the ratio of Fe and N in the Fe_4N layer (5.2:1) slightly deviate from the stoichiometric condition of 4:1.

Magneto-transport study of MTJs

The magneto-transport measurements have been performed by a dc two-probe configuration, where the negative bias corresponds to the electrons tunneling from the top to bottom electrode **(Fig. 2(a)).** Although there are two $MgAlO_x$ insulating layers in the structure, the junction resistance is mainly dominated by the thicker one. **Figs. 2(b,c)** show the TMR curves measured at RT and 10K for bias voltages V=+0.45V and V=-0.6V, respectively. It is interesting to find that the TMR sign can be reversed with different voltages. At 300K, the TMR can be modulated from -27% to +3%. At 10K, the TMR sign reversal effect is enhanced from -40% to +5%. Here, both positive and negative TMR has been calculated by the definition of TMR ratio=$(R_{AP}-R_P)/R_P\times100\%$, where R_P and R_{AP} are the junction resistance when the magnetizations of both electrodes beside the tunneling barrier are in parallel (P) and antiparallel (AP) configurations, respectively. This definition limits the negative TMR ratio up to 100%. Under optimistic definition (TMR ratio=$(R_{AP}-R_P)/R_{AP}\times100\%$)), our maximum negative TMR is -70% at 10K and -38% at 300K, which is approaching the reported highest negative TMR ratios (-75%) in CoFeB/MgO/Fe_4N MTJs.[33,34] However, no TMR sign change has been observed in those systems.[33,34] In the TMR curves at 10K, it is found that the AP plateaus are not well established with an asymmetric form at positive and negative magnetic field. This could be due to the

complicated magnetic structure in Fe_4N, which has a partial out-of-plane magnetic component[29] (see **SI Note 5**). **Fig. 2(d)** shows the resistance in P and AP states as a function of temperature for V=+0.45V and V=-0.6V. The corresponding variation of TMR as a function of temperature is shown in **Fig. 2(e)** (see more details in **SI Note 6**). It is found that the resistance of junction gradually reduces with increase of temperature. However, the variation of resistance is lower than 25% for the largest case, which is an important signature to exclude either pinhole dominated tunneling for thin barrier (increased resistance with T)[35] or hopping dominated tunneling through homogenous localized defect states in thick barrier (exponentially reduced resistance with increasing T).[25] Although inelastic tunneling through inhomogeneous defects may result in a small temperature dependence,[17] it should be significantly reduced at low temperature. Therefore, our TMR at low temperature is mainly dominated by coherent direct tunneling or elastic tunneling.

To have more insight on the TMR sign change for the Fe/$MgAlO_x$/Fe_4N MTJ, we measured TMR values at different bias at 10K, as shown in the blue dots in **Fig. 2(f)** (see more details in **SI Note 7**). It is clearly that TMR changes its sign at about -0.2 V. Below this voltage, TMR almost keeps constant with positive TMR around +5%. Above -0.2 V, the TMR becomes negative and the value varies a lot with a maximum at +0.5V. For comparison, we have also plotted the TMR values from a Fe/MgO/Fe_4N MTJ (red dots in **Fig. 2(f)**). Both samples show the same trend of TMR sign change, but the negative TMR ratio of MTJ with MgO barrier is only half of that with $MgAlO_x$ barrier. Please find more characterizations of MTJs with MgO barrier in **SI Note 8**. The superior performance of $MgAlO_x$ based MTJ could be attributed to the better lattice mismatch between Fe_4N and $MgAlO_x$ as well as less N diffusion inside the barrier which have been observed in the above STEM characterizations.

To further understand the bias-dependent TMR, we set the MTJ into P and AP states respectively

by applying appropriate in-plane field, and measured the bias dependence of differential conductance dI/dV at different temperatures (**Figs. 3 (a,b)**). All dI/dV curves in both states have been normalized by G_p (V=0, T=10 K). **Fig. 3(c)** shows the normalized differential conductance for both states at 10K. When V<-0.1V, G_p is always higher than G_{ap}, resulting a positive TMR. However, when 0V<V<0.3V G_{ap} increases faster than G_p, resulting a large negative TMR. At V>0.3V, the increase of G_p becomes more important than G_{ap}, which effectively reduces the negative TMR. **Fig. 3(d)** displays the bias dependence of TMR deduced by the I-V curves (R=V/I) at different temperatures, showing a good agreement with the bias dependent TMR ratios measured directly from the R-H curves in **Fig. 2(f)**. The large attenuation of negative TMR with temperature can be found, which is mainly due to the large increase of G_p while G_{ap} almost keeps constant with the temperature, as shown in **Figs. 3(a,b)**.

It is noticed that there are some small conductance oscillations appearing when V<0V in **Fig. 3 (a-c)** in both P and AP states. These oscillations can be explained by the electron tunneling in the quantum well (QW) states formed in the $MgAlO_x$/Fe/$MgAlO_x$ structure. However, the oscillation amplitudes are much smaller than that observed in our previous studied single or double QW MTJs with all Fe electrodes[36,37] (see **SI Note 9**). This can be understood that the top Fe_4N electrode has no majority electrons with Δ_1 symmetry at the Fermi level (E_F) to match the bottom Fe QW states (formed by majority Δ_1 bands).[36,37] The main origin of TMR sign change should not be related to the QW states since similar variation of conductance in P and AP states can also be evidenced in MgO based MTJ where there is no QW structure (see **SI Note 8**).

In addition, it is well-known that for MBE samples the feature in dI/dV at -0.2 V could be due to the interface resonance state (IRS) at Fe/MgO interface.[38] To clarify if IRS plays a role on the transport properties, we have conducted the inelastic electron tunneling spectroscopy (IETS) experiments through the derivative of the dynamic conductance (d^2I/dV^2). However, no IRS signature

can be found at the MgO/Fe_4N, $MgAlO_x$/Fe_4N, or Fe/$MgAlO_x$ interfaces, thus excluding the influence of IRS on TMR reversal (see **SI Note 10**).

Since N diffusion inside the barrier could lead to the creation of inhomogeneous defects, we should also consider the possibility of TMR reversal due to the inelastic tunneling through these defects. Indeed, the inelastic tunneling through inhomogeneous localized states inside the barrier could potentially lead to a similar TMR sign reversal effect.[17,39] However, the observed TMR ratio and TMR sign reversal effect are highly device-specific, given that the defects introduced in the barrier during growth are highly random. Moreover, to observe such inversion of TMR due to the localized defect states, the junction area must be sufficiently small, displaying two-level fluctuations of electric current and indicating impurity/defect-driven transport.[40] On the contrary, for large-size junctions (ranging from a fraction of μm^2 to a few mm^2), the resultant conductance is the sum over a large number of local disorder configurations. On average, this leads to a reduction in TMR, and the TMR sign reversal is no longer observed.[41] In our case, our junction has a relatively large area (10×10 to 40×40 μm^2) with high structural quality and homogeneity. Additionally, MTJs with different barriers (MgO or $MgAlO_x$) exhibit almost identical TMR reversal behavior. Therefore, the mechanism involving inelastic tunneling through inhomogeneous defects should be excluded.

First principle calculations of the band structure

To understand the origin of the V dependence of TMR ratio, first principle calculations have been performed to investigate the coherent tunneling in MTJ closely linked with the spin and symmetry of the electrons in both electrodes. Since Fe and Fe_4N have different crystalline structures, we have defined the Γ-X in the band structure for the transport direction ($k_{//}$=0) in both cases for the reason of uniformity. **Fig. 4(a)** shows the symmetry and spin-resolved band structures along transport direction (Γ-X) for bulk Fe and Fe_4N. For bcc Fe, the majority-spin Δ_1 band crosses the Fermi level

while the minority-spin Δ_1 band situates well above E_F, which reveals a half-metal nature in terms of Δ_1 state along the transport direction.[42] For Fe_4N, the minority Δ_1 and Δ_5 bands cross the Fermi level, while no majority bands cross E_F along the transport direction, which is in a good agreement with the calculations reported by Yang *et al.*[28] This indicates that Fe_4N also reveals a half-metal nature in terms of both Δ_1 and Δ_5 states. Since in single crystal Fe(001)/MgO/Fe[43] or Fe(001)/$MgAl_2O_4$/Fe[44] MTJs, MgO and $MgAl_2O_4$ tunneling barriers can efficiently filter electrons with other symmetries than Δ_1 and Δ_5 bands, it is reasonable to consider that only the Δ_1 and Δ_5 bands are mainly involved in the tunneling process. Previous theoretical work in Fe_4N/MgO/Fe_4N MTJ also reveals that not only the Δ_1 band but also Δ_5 band electrons play an important role for the symmetry dependent coherent transmission.[28]

To make the analysis clear, the symmetry and spin-resolved DOS for $k_{//}=0$ of Fe and Fe_4N is plotted in **Figs. 4(b-e)** as a function of the energy. Generally, the conductance is created by the electrons tunneling from an occupied band of one electrode to the unoccupied band of the other electrode. Therefore, the conductance of the P state is determined by: Majority (↑) to Majority (↑) and Minority (↓) to Minority (↓) band tunneling while the conductance of the AP state is determined by: Majority (↑) to Minority (↓) and Minority (↓) to Majority (↑) band tunneling.

Figs. 4(b,c) show the tunneling through Δ_1 and Δ_5 bands under positive bias, respectively. Since there are no DOS near the Fermi energy for the majority bands of Fe_4N, the tunneling channels when $V>0$V are mainly from: (1) Fe $\Delta_1\uparrow$ to Fe_4N $\Delta_1\downarrow$, (2) Fe $\Delta_5\uparrow$ to Fe_4N $\Delta_5\downarrow$ for AP conductance and (3) Fe $\Delta_5\downarrow$ to Fe_4N $\Delta_5\downarrow$ for P conductance. From **Fig. 3(c)**, we know that the normalized dI/dV in the AP state increases fast first when $0<V<0.2$ V, then slows down when 0.2 V$<V<$0.4 V, and increases fast again when $V>0.4$ V. This fast-slow-fast increase of conductance is well attributed to the strong Fe_4N $\Delta_1\downarrow$ peak around 0.2 V in the AP tunneling channel (1), as shown in **Fig. 4(b)**. Notice that the channel

(2) is less important since the DOS of Fe_4N $\Delta_5\downarrow$ near E_F is smaller than that of Fe_4N $\Delta_1\downarrow$. The low DOS intensity in Fe_4N $\Delta_5\downarrow$ also limits the P conductance channel (3). This can well explain the observed large negative TMR ratio. In **Figs. 3(a,b)**, the temperature dependence of conductance shows that AP conductance almost keeps constant, while P conductance increases with temperature at positive bias. This results in the rapid decrease of negative TMR with increase of *T*, which can be understood as following. Since the thermal effect induces the phonon scattering, the distribution of DOS as a function of the energy will be smeared. Therefore, the conductance in channel (1) reduces while that in channels (2) and (3) increases, so that channels (1) and (2) compensate together resulting in a small variation of the AP conductance while the P conductance increases with the increase of conductance in channel (3).

Under negative bias as shown in **Figs. 4(d,e)**, the tunneling channels are mainly from: (4) Fe_4N $\Delta_1\downarrow$ to Fe $\Delta_1\uparrow$ and (5) Fe_4N $\Delta_5\downarrow$ to Fe $\Delta_5\uparrow$ for AP conductance and (6) Fe_4N $\Delta_5\downarrow$ to Fe $\Delta_5\downarrow$ for P conductance. From **Fig. 3(c)**, the changes of the normalized dI/dV under negative bias are similar in the AP and P states, and the normalized dI/dV in the P state is slightly higher than that in the AP state. From **Figs. 4(d,e)**, the AP conductance is mainly determined by the channel (4) since the DOS of Fe $\Delta_5\uparrow$ in channel (5) decreases rapidly with higher energy. By comparison of channels (4) and (6) for AP and P conductance, the DOS of the Fe $\Delta_5\downarrow$ in (6) is larger than that of Fe $\Delta_1\uparrow$ in (4). This can explain the higher P conductance observed in normalized dI/dV curves in **Fig. 3(c)**, which results in the positive TMR ratio. However, since there is no distinguished DOS peak in Fe $\Delta_5\downarrow$, the positive TMR ratio is less pronounced than the negative TMR ratio. Here, we can qualitatively explain the experimental observation by the simple analyses based on the band structure of bulk Fe_4N and Fe. A more rigorous model should be taken into account the electrodes, barrier and interfaces together, which will give more insight of the transport process.

Conclusion

In summary, we have fabricated epitaxial Fe/$MgAlO_x$/Fe_4N MTJs by MBE growth. The voltage-controlled and sign-reversible TMR effect is demonstrated from 10 K to 300 K. At RT, the positive TMR ratio of +3.2% at V=−0.6 V can be changed to the negative TMR ratio of −26.7% (−38% under the optimistic definition) at V=+0.45 V. The voltage-dependence of TMR ratio can be well explained by a simple model taking account of the symmetry and spin-resolved band structures of Fe and Fe_4N. This new freedom of TMR turnability paves a way for the development of new spintronic devices for real-time reprogrammable spin logic gate applications.

Methods

Sample preparation

The main stack MgO(001)||MgO(10 nm)/Fe(45 nm)/$MgAlO_x$(0.6 nm)/Fe(7 nm)/$MgAlO_x$(2.5 nm)/Fe_4N(3 nm)/Co(20 nm)/Au(10 nm) was deposited in a MBE system with a base pressure better than 1×10^{-10} torr. Firstly, the substrate was annealed at 700°C for 60 mins and 10 nm MgO seed layer was deposited. Then the first 45 nm thick Fe layer was deposited at RT by e-beam evaporation and annealed *in situ* at 600°C for 30 mins to smooth the surface. The first 0.6 nm thick $MgAlO_x$ barrier was grown at about 70°C and the growth process was monitored by reflection high-energy electron diffraction (RHEED, see **SI Note 1**). Two-dimensional layer-by-layer growth of $MgAlO_x$ was observed by RHEED intensity oscillation. The second 7 nm thick Fe layer was deposited at about 70°C and annealed *in situ* at 500°C for 20 mins followed by a deposition of 2.5 nm thick $MgAlO_x$ barrier. During the growth of Fe_4N films on $MgAlO_x$, the Fe source was heated to 1250°C by Knudsen cell, and the substrate temperature was kept at 400°C with a nitrogen partial pressure of 2×10^{-5} Torr in the MBE chamber. The PCS-ECR (plasma cracker source - electron cyclotron resonance) source

was used with the following characteristics: V_{anode}=400 V, $V_{extractor}$=-200 V, $I_{magnetron}$=40 mA. Finally, 20 nm thick Co layer was deposited above the Fe_4N layer to enhance the coercivity and 10 nm thick Au was used to prevent the films from oxidation. A control stack MgO(001)//MgO(10 nm)/Fe(45 nm)/MgO(2.5 nm)/Fe_4N(3 nm)/Co(20 nm)/Au(10 nm) was also deposited through a similar procedure. More detailed MTJ growth can be found elsewhere.[36,37,43]

The multilayers were then patterned into junctions with the area size varying from 10×10 to 40×40μm^2 by standard ultraviolet lithography combined with Ar^+ ion etching. The transport measurements were carried out in a cryostat (cooled by liquid helium) with electrical magnets. A Keithley 2450 was used to apply the bias voltage to the MTJ and probe the current accordingly.

First principle calculations

The first principle calculations were performed using the projector-augmented-wave (PAW) method[45] as implemented in the Vienna *ab initio* simulation package (VASP).[46–48] An energy cutoff of 500 eV and Perdew-Burke-Ernzerhof generalized-gradient approximation (GGA-PBE)[49] for the exchange-correlation function were used throughout. A 21×21×21 *k*-point mesh are performed for structural relaxations and self-consistent calculations for Fe_4N until the force on each atom is smaller than 0.01 eV/Å and the total energy is converged to be less than 1×10^{-5} eV. The bulk Fe_4N has a cubic antiperovskite structure and the experimental lattice constant is 3.795 Å. We also calculate the bcc Fe to analyze the tunneling between these two electrodes.

STEM-EELS characterization

HR-STEM combined with spatially resolved EELS was performed by using a probe-corrected microscope JEOL ARM200F (cold FEG) equipped with a GATAN GIF quantum energy filter to

reveal the structure and element distribution. The microscope was operated at 200 kV. High angle annular dark-field (HAADF), annular dark-field (ADF) and bright-field (BF) images were simultaneously recorded for investigating the heterostructure while only HAADF signal was recorded during EELS mapping. EELS spectrum images were recorded with a probe current of about 50 pA. Two EELS spectrum images were simultaneously recorded: one for the low-loss part containing the zero-loss, the other for the core loss, which allows advanced data post processing (correction of energy drift, multiple scattering corrections). A multivariate statistical analysis software (temDM MSA) was used to improve the quality of the STEM-EELS data by de-noising the core-loss spectrum images before its processing to draw quantitative chemical maps.[50] Thin lamellas were extracted by focused ion beam (FIB) milling using an FEI Helios Nanolab 600i dual beam.

Acknowledgement

We acknowledge Ludovic Pasquier for the support of MBE growth. This work is supported by French National Research Agency (ANR) SOTspinLED (No. ANR-22-CE24-0006-01) project. Experiments were performed using equipments from the platform TUBE-Davm and the platform CCMEM both funded by FEDER (EU), ANR, the Region Lorraine and Grand Nancy.

Supporting Information

RHEED patterns of the MTJ with $MgAlO_x$ barrier; RHEED patterns of the MTJ with MgO barrier; Lattice mismatch of Fe_4N/MgO and Fe_4N/$MgAlO_x$; Structure characterization of the MTJ with MgO barrier; Magnetic properties of Fe_4N layer; Temperature dependence of the TMR ratio of the MTJ with $MgAlO_x$ barrier; Bias dependence of the TMR measurements of the MTJ with $MgAlO_x$ barrier; Bias dependence of TMR of the MTJ with MgO barrier; Elimination of the QW structure's influence on TMR enhancement; Elimination of the interface resonant states' influence on TMR

reversal.

References

(1) Han, X.; Wang, X.; Wan, C.; Yu, G.; Lv, X. Spin-Orbit Torques: Materials, Physics, and Devices. *Appl. Phys. Lett.* **2021**, *118* (12), 120502. https://doi.org/10.1063/5.0039147.

(2) Miyazaki, T.; Tezuka, N. Giant Magnetic Tunneling Effect in Fe/Al2o3/Fe Junction. *J. Magn. Magn. Mater.* **1995**, *139* (3), L231–L234. https://doi.org/10.1016/0304-8853(95)90001-2.

(3) Moodera, J.; Kinder, L.; Wong, T.; Meservey, R. Large Magnetoresistance at Room-Temperature in Ferromagnetic Thin-Film Tunnel-Junctions. *Phys. Rev. Lett.* **1995**, *74* (16), 3273–3276. https://doi.org/10.1103/PhysRevLett.74.3273.

(4) Parkin, S. S. P.; Kaiser, C.; Panchula, A.; Rice, P. M.; Hughes, B.; Samant, M.; Yang, S. H. Giant Tunnelling Magnetoresistance at Room Temperature with MgO (100) Tunnel Barriers. *Nat. Mater.* **2004**, *3* (12), 862–867. https://doi.org/10.1038/nmat1256.

(5) Kong, W. J.; Wan, C. H.; Guo, C. Y.; Fang, C.; Tao, B. S.; Wang, X.; Han, X. F. All-Electrical Manipulation of Magnetization in Magnetic Tunnel Junction via Spin-Orbit Torque. *Appl. Phys. Lett.* **2020**, *116* (16). https://doi.org/10.1063/5.0001758.

(6) Honjo, H.; Nguyen, T. V. A.; Watanabe, T.; Nasuno, T.; Zhang, C.; Tanigawa, T.; Miura, S.; Inoue, H.; Niwa, M.; Yoshiduka, T.; Noguchi, Y.; Yasuhira, M.; Tamakoshi, A.; Natsui, M.; Ma, Y.; Koike, H.; Takahashi, Y.; Furuya, K.; Shen, H.; Fukami, S.; Sato, H.; Ikeda, S.; Hanyu, T.; Ohno, H.; Endoh, T. First Demonstration of Field-Free SOT-MRAM with 0.35 Ns Write Speed and 70 Thermal Stability under 400°C Thermal Tolerance by Canted SOT Structure and Its Advanced Patterning/SOT Channel Technology. In *2019 IEEE International Electron Devices Meeting (IEDM)*; 2019; p 28.5.1-28.5.4. https://doi.org/10.1109/IEDM19573.2019.8993443.

(7) Garello, K.; Yasin, F.; Hody, H.; Couet, S.; Souriau, L.; Sharifi, S. H.; Swerts, J.; Carpenter, R.; Rao, S.; Kim, W.; Wu, J.; Sethu, K. K. V.; Pak, M.; Jossart, N.; Crotti, D.; Furnemont, A.; Kar, G. S. Manufacturable 300mm Platform Solution for Field-Free Switching SOT-MRAM. In *2019 Symposium on VLSI Circuits*; IEEE: New York, 2019; pp T194–T195.

(8) Jin, Z.; Mohd Noor Sam, M. A. I.; Oogane, M.; Ando, Y. Serial MTJ-Based TMR Sensors in Bridge Configuration for Detection of Fractured Steel Bar in Magnetic Flux Leakage Testing. *Sensors* **2021**, *21* (2), 668. https://doi.org/10.3390/s21020668.

(9) Zhao, W.; Chappert, C.; Javerliac, V.; Noziere, J.-P. High Speed, High Stability and Low Power Sensing Amplifier for MTJ/CMOS Hybrid Logic Circuits. *IEEE Trans. Magn.* **2009**, *45* (10), 3784–3787. https://doi.org/10.1109/TMAG.2009.2024325.

(10) Torrejon, J.; Riou, M.; Araujo, F. A.; Tsunegi, S.; Khalsa, G.; Querlioz, D.; Bortolotti, P.; Cros, V.; Yakushiji, K.; Fukushima, A.; Kubota, H.; Uasa, S. Y.; Stiles, M. D.; Grollier, J. Neuromorphic Computing with Nanoscale Spintronic Oscillators. *Nature* **2017**, *547* (7664), 428–431. https://doi.org/10.1038/nature23011.

(11) Borders, W. A.; Pervaiz, A. Z.; Fukami, S.; Camsari, K. Y.; Ohno, H.; Datta, S. Integer Factorization Using Stochastic Magnetic Tunnel Junctions. *Nature* **2019**, *573* (7774), 390–393. https://doi.org/10.1038/s41586-019-1557-9.

(12) Ney, A.; Pampuch, C.; Koch, R.; Ploog, K. H. Programmable Computing with a Single Magnetoresistive Element. *Nature* **2003**, *425* (6957), 485–487. https://doi.org/10.1038/nature02014.

(13) Wan, C.; Zhang, X.; Yuan, Z.; Fang, C.; Kong, W.; Zhang, Q.; Wu, H.; Khan, U.; Han, X. Programmable Spin Logic Based on Spin Hall Effect in a Single Device. *Adv. Electron. Mater.* **2017**, *3* (3), 1600282. https://doi.org/10.1002/aelm.201600282.

(14) Wang, X.; Wan, C.; Kong, W.; Zhang, X.; Xing, Y.; Fang, C.; Tao, B.; Yang, W.; Huang, L.; Wu,

H.; Irfan, M.; Han, X. Field-Free Programmable Spin Logics via Chirality-Reversible Spin-Orbit Torque Switching. *Adv. Mater.* **2018**, *30* (31), 1801318. https://doi.org/10.1002/adma.201801318.

(15) Thomas, A.; Meyners, D.; Ebke, D.; Liu, N.-N.; Sacher, M. D.; Schmalhorst, J.; Reiss, G.; Ebert, H.; Huetten, A. Inverted Spin Polarization of Heusler Alloys for Spintronic Devices. *Appl. Phys. Lett.* **2006**, *89* (1), 012502. https://doi.org/10.1063/1.2219333.

(16) Sharma, M.; Wang, S. X.; Nickel, J. H. Inversion of Spin Polarization and Tunneling Magnetoresistance in Spin-Dependent Tunneling Junctions. *Phys. Rev. Lett.* **1999**, *82* (3), 616–619. https://doi.org/10.1103/PhysRevLett.82.616.

(17) Tsymbal, E. Y.; Sokolov, A.; Sabirianov, I. F.; Doudin, B. Resonant Inversion of Tunneling Magnetoresistance. *Phys. Rev. Lett.* **2003**, *90* (18), 186602. https://doi.org/10.1103/PhysRevLett.90.186602.

(18) Vera Marun, I. J.; Postma, F. M.; Lodder, J. C.; Jansen, R. Tunneling Magnetoresistance with Positive and Negative Sign in La0.67Sr0.33MnO3/SrTiO3/Co Junctions. *Phys. Rev. B* **2007**, *76* (6), 064426. https://doi.org/10.1103/PhysRevB.76.064426.

(19) Greullet, F.; Snoeck, E.; Tiusan, C.; Hehn, M.; Lacour, D.; Lenoble, O.; Magen, C.; Calmels, L. Large Inverse Magnetoresistance in Fully Epitaxial Fe/Fe3O4/MgO/Co Magnetic Tunnel Junctions. *Appl. Phys. Lett.* **2008**, *92* (5), 053508. https://doi.org/10.1063/1.2841812.

(20) Marnitz, L.; Rott, K.; Niehoerster, S.; Klewe, C.; Meier, D.; Fabretti, S.; Witziok, M.; Krampf, A.; Kuschel, O.; Schemme, T.; Kuepper, K.; Wollschlaeger, J.; Thomas, A.; Reiss, G.; Kuschel, T. Sign Change in the Tunnel Magnetoresistance of Fe3O4/MgO/Co-Fe-B Magnetic Tunnel Junctions Depending on the Annealing Temperature and the Interface Treatment. *AIP Adv.* **2015**, *5* (4), 047103. https://doi.org/10.1063/1.4917018.

(21) Yasui, S.; Honda, S.; Okabayashi, J.; Yanase, T.; Shimada, T.; Nagahama, T. Large Inverse Tunnel Magnetoresistance in Magnetic Tunnel Junctions with an Fe3O4 Electrode. *Phys. Rev. Appl.* **2021**, *15* (3), 034042. https://doi.org/10.1103/PhysRevApplied.15.034042.

(22) Pantel, D.; Goetze, S.; Hesse, D.; Alexe, M. Reversible Electrical Switching of Spin Polarization in Multiferroic Tunnel Junctions. *Nat. Mater.* **2012**, *11* (4), 289–293. https://doi.org/10.1038/NMAT3254.

(23) Liang, S.; Yang, H.; Yang, H.; Tao, B.; Djeffal, A.; Chshiev, M.; Huang, W.; Li, X.; Ferri, A.; Desfeux, R.; Mangin, S.; Lacour, D.; Hehn, M.; Copie, O.; Dumesnil, K.; Lu, Y. Ferroelectric Control of Organic/Ferromagnetic Spinterface. *Adv. Mater.* **2016**, *28* (46), 10204–10210. https://doi.org/10.1002/adma.201603638.

(24) Liang, S.; Yu, Z.; Devaux, X.; Ferri, A.; Huang, W.; Yang, H.; Desfeux, R.; Li, X.; Migot, S.; Chaudhuri, D.; Yang, H.; Chshiev, M.; Yang, C.; Zhou, B.; Fang, J.; Mangin, S.; Lu, Y. Quenching of Spin Polarization Switching in Organic Multiferroic Tunnel Junctions by Ferroelectric "Ailing-Channel" in Organic Barrier. *ACS Appl. Mater. Interfaces* **2018**, *10* (36), 30614–30622. https://doi.org/10.1021/acsami.8b11437.

(25) Lu, Y.; Tran, M.; Jaffrès, H.; Seneor, P.; Deranlot, C.; Petroff, F.; George, J.-M.; Lépine, B.; Ababou, S.; Jézéquel, G. Spin-Polarized Inelastic Tunneling through Insulating Barriers. *Phys. Rev. Lett.* **2009**, *102* (17), 176801. https://doi.org/10.1103/PhysRevLett.102.176801.

(26) Kokado, S.; Fujima, N.; Harigaya, K.; Shimizu, H.; Sakuma, A. Theoretical Analysis of Highly Spin-Polarized Transport in the Iron Nitride Fe4N. *Phys. Rev. B* **2006**, *73* (17), 172410. https://doi.org/10.1103/PhysRevB.73.172410.

(27) Li, H.; Li, X.; Kim, D.; Zhao, G.; Zhang, D.; Diao, Z.; Chen, T.; Wang, J.-P. High Spin Polarization in Epitaxial Fe4N Thin Films Using Cr and Ag as Buffer Layers. *Appl. Phys. Lett.*

2018, *112* (16), 162407. https://doi.org/10.1063/1.5023698.
(28) Yang, B.; Tao, L.; Jiang, L.; Chen, W.; Tang, P.; Yan, Y.; Han, X. Ultrahigh Tunneling-Magnetoresistance Ratios in Nitride-Based Perpendicular Magnetic Tunnel Junctions from First Principles. *Phys. Rev. Appl.* **2018**, *9* (5), 54019. https://doi.org/10.1103/PhysRevApplied.9.054019.
(29) Li, H.; Wang, G.; Li, D.; Hu, P.; Zhou, W.; Dang, S.; Ma, X.; Dai, T.; Kang, S.; Yu, F.; Zhou, X.; Wu, S.; Li, S. Field-Free Deterministic Magnetization Switching with Ultralow Current Density in Epitaxial Au/Fe4N Bilayer Films. *ACS Appl. Mater. Interfaces* **2019**, *11* (18), 16965–16971. https://doi.org/10.1021/acsami.9b00129.
(30) Li, H.; Wang, G.; Li, D.; Hu, P.; Zhou, W.; Ma, X.; Dang, S.; Kang, S.; Dai, T.; Yu, F.; Zhou, X.; Wu, S.; Li, S. Spin-Orbit Torque-Induced Magnetization Switching in Epitaxial Au/Fe4N Bilayer Films. *Appl. Phys. Lett.* **2019**, *114* (9), 092402. https://doi.org/10.1063/1.5078395.
(31) Mi, W. B.; Guo, Z. B.; Feng, X. P.; Bai, H. L. Reactively Sputtered Epitaxial γ'-Fe4N Films: Surface Morphology, Microstructure, Magnetic and Electrical Transport Properties. *Acta Mater.* **2013**, *61* (17), 6387–6395. https://doi.org/10.1016/j.actamat.2013.07.016.
(32) Haynes, W. M. *CRC Handbook of Chemistry and Physics*; CRC press, 2016.
(33) Sunaga, K.; Tsunoda, M.; Komagaki, K.; Uehara, Y.; Takahashi, M. Inverse Tunnel Magnetoresistance in Magnetic Tunnel Junctions with an Fe4N Electrode. *J. Appl. Phys.* **2007**, *102* (1), 013917. https://doi.org/10.1063/1.2753576.
(34) Komasaki, Y.; Tsunoda, M.; Isogami, S.; Takahashi, M. 75% Inverse Magnetoresistance at Room Temperature in Fe4N/MgO/CoFeB Magnetic Tunnel Junctions Fabricated on Cu Underlayer. *J. Appl. Phys.* **2009**, *105* (7), 07C928. https://doi.org/10.1063/1.3072827.
(35) Åkerman, J. J.; Escudero, R.; Leighton, C.; Kim, S.; Rabson, D. A.; Dave, R. W.; Slaughter, J. M.; Schuller, I. K. Criteria for Ferromagnetic–Insulator–Ferromagnetic Tunneling. *Journal of Magnetism and Magnetic Materials* **2002**, *240* (1–3), 86–91. https://doi.org/10.1016/S0304-8853(01)00712-0.
(36) Tao, B. S.; Yang, H. X.; Zuo, Y. L.; Devaux, X.; Lengaigne, G.; Hehn, M.; Lacour, D.; Andrieu, S.; Chshiev, M.; Hauet, T.; Montaigne, F.; Mangin, S.; Han, X. F.; Lu, Y. Long-Range Phase Coherence in Double-Barrier Magnetic Tunnel Junctions with a Large Thick Metallic Quantum Well. *Phys. Rev. Lett.* **2015**, *115* (15), 157204. https://doi.org/10.1103/PhysRevLett.115.157204.
(37) Tao, B.; Wan, C.; Tang, P.; Feng, J.; Wei, H.; Wang, X.; Andrieu, S.; Yang, H.; Chshiev, M.; Devaux, X.; Hauet, T.; Montaigne, F.; Mangin, S.; Hehn, M.; Lacour, D.; Han, X.; Lu, Y. Coherent Resonant Tunneling through Double Metallic Quantum Well States. *Nano Lett.* **2019**, *19* (5), 3019–3026. https://doi.org/10.1021/acs.nanolett.9b00205.
(38) Zermatten, P.-J.; Gaudin, G.; Maris, G.; Miron, M.; Schuhl, A.; Tiusan, C.; Greullet, F.; Hehn, M. Experimental Evidence of Interface Resonance States in Single-Crystal Magnetic Tunnel Junctions. *Phys. Rev. B* **2008**, *78* (3), 033301. https://doi.org/10.1103/PhysRevB.78.033301.
(39) Tsymbal, E. Yu.; Pettifor, D. G. Spin-Polarized Electron Tunneling across a Disordered Insulator. *Phys. Rev. B* **1998**, *58* (1), 432–437. https://doi.org/10.1103/PhysRevB.58.432.
(40) Doudin, B.; Redmond, G.; Gilbert, S. E.; Ansermet, J.-Ph. Magnetoresistance Governed by Fluctuations in Ultrasmall Ni/NiO/Co Junctions. *Phys. Rev. Lett.* **1997**, *79* (5), 933–936. https://doi.org/10.1103/PhysRevLett.79.933.
(41) Miyazaki, T.; Tezuka, N. Spin Polarized Tunneling in Ferromagnet/Insulator/Ferromagnet Junctions. *Journal of Magnetism and Magnetic Materials* **1995**, *151* (3), 403–410. https://doi.org/10.1016/0304-8853(95)00563-3.
(42) Kisker, E.; Schröder, K.; Gudat, W.; Campagna, M. Spin-Polarized Angle-Resolved

Photoemission Study of the Electronic Structure of Fe(100) as a Function of Temperature. *Phys. Rev. B* **1985**, *31* (1), 329–339. https://doi.org/10.1103/PhysRevB.31.329.

(43) Lu, Y.; Yang, H.-X.; Tiusan, C.; Hehn, M.; Chshiev, M.; Duluard, A.; Kierren, B.; Lengaigne, G.; Lacour, D.; Bellouard, C.; Montaigne, F. Spin-Orbit Coupling Effect by Minority Interface Resonance States in Single-Crystal Magnetic Tunnel Junctions. *Phys. Rev. B* **2012**, *86* (18), 184420. https://doi.org/10.1103/PhysRevB.86.184420.

(44) Miura, Y.; Muramoto, S.; Abe, K.; Shirai, M. First-Principles Study of Tunneling Magnetoresistance in Fe/MgAl2O4/Fe(001) Magnetic Tunnel Junctions. *Phys. Rev. B* **2012**, *86* (2), 024426. https://doi.org/10.1103/PhysRevB.86.024426.

(45) Blochl, P. Projector Augmented-Wave Method. *Phys. Rev. B* **1994**, *50* (24), 17953–17979. https://doi.org/10.1103/PhysRevB.50.17953.

(46) Kresse, G.; Hafner, J. Ab Initio Molecular Dynamics for Liquid Metals. *Phys. Rev. B* **1993**, *47* (1), 558–561. https://doi.org/10.1103/PhysRevB.47.558.

(47) Kresse, G.; Furthmuller, J. Efficiency of Ab-Initio Total Energy Calculations for Metals and Semiconductors Using a Plane-Wave Basis Set. *Comput. Mater. Sci.* **1996**, *6* (1), 15–50. https://doi.org/10.1016/0927-0256(96)00008-0.

(48) Kresse, G.; Furthmuller, J. Efficient Iterative Schemes for Ab Initio Total-Energy Calculations Using a Plane-Wave Basis Set. *Phys. Rev. B* **1996**, *54* (16), 11169–11186. https://doi.org/10.1103/PhysRevB.54.11169.

(49) Perdew, J. P.; Burke, K.; Ernzerhof, M. Generalized Gradient Approximation Made Simple. *Phys. Rev. Lett.* **1996**, *77* (18), 3865–3868. https://doi.org/10.1103/PhysRevLett.77.3865.

(50) Potapov, P. Why Principal Component Analysis of STEM Spectrum-Images Results in "Abstract", Uninterpretable Loadings? *Ultramicroscopy* **2016**, *160*, 197–212. https://doi.org/10.1016/j.ultramic.2015.10.020.

Figures

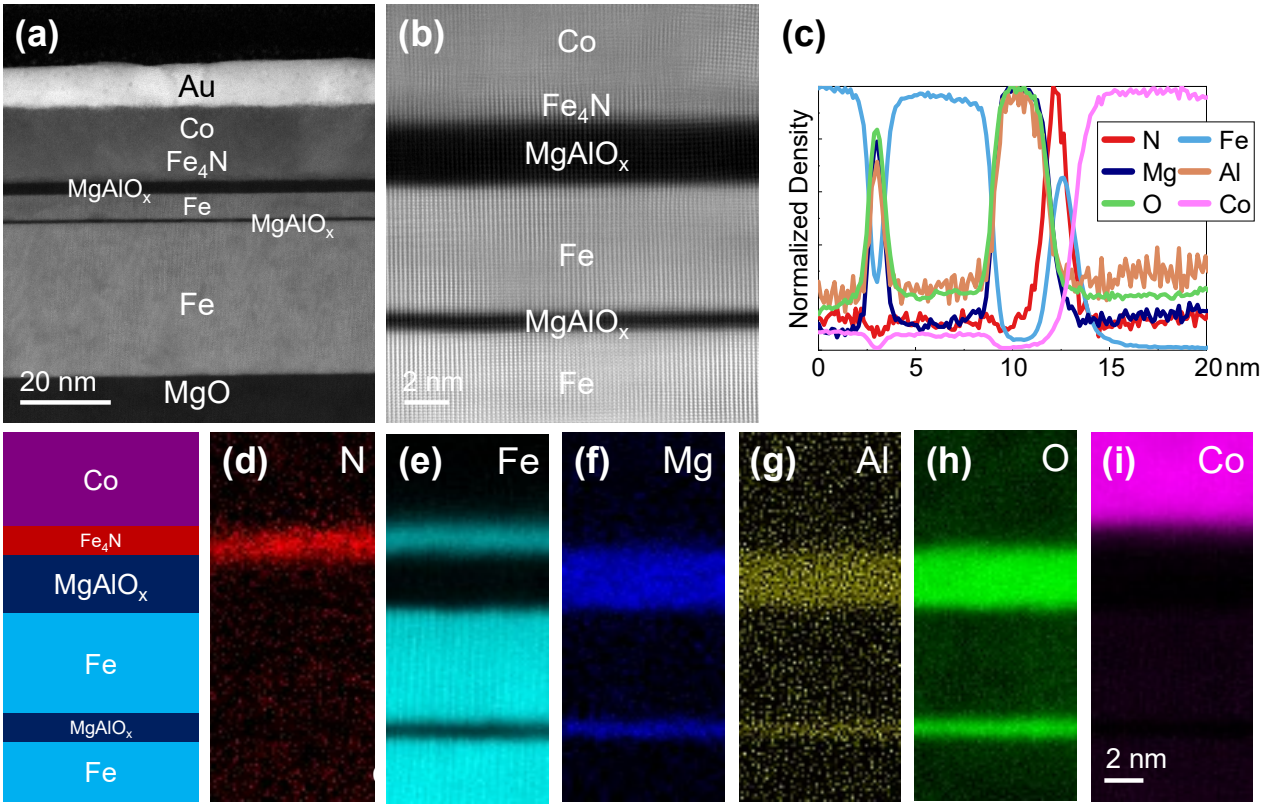

Figure 1: Interfacial structures and chemical maps of MTJ stack. STEM-HAADF images with different scales are shown in (a) and (b). Normalized elements density profiles and elements maps extracted from STEM-EELS are shown in (c) and (d-i), respectively.

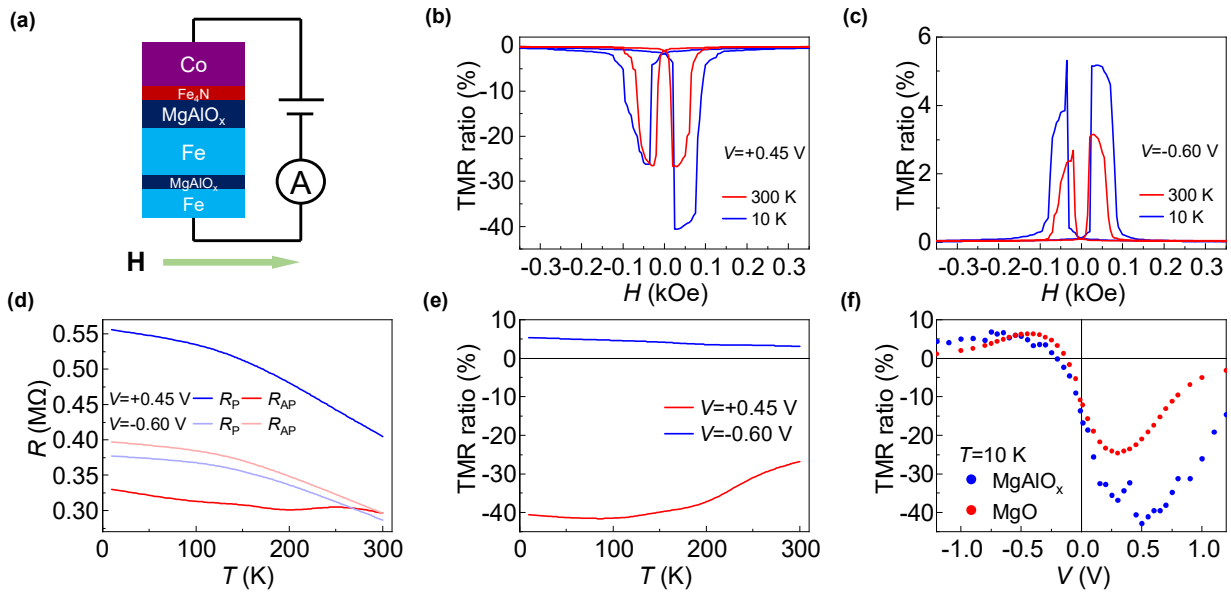

Figure 2: TMR measurement results of the Fe/$MgAlO_x$/Fe_4N MTJ. (a) Schematic of the measurement setup. (b,c) TMR curves measured at RT and 10 K for bias voltage (b) V=+0.45 V and (c) V=−0.60 V, respectively. (d) Temperature dependence of the P and AP state resistance when V=+0.45 V and −0.60 V. (e) Temperature dependence of the TMR ratios when V=+0.45 V and −0.60 V. (f) Bias dependence of TMR ratios of Fe_4N MTJs with $MgAlO_x$ and MgO barriers at 10 K.

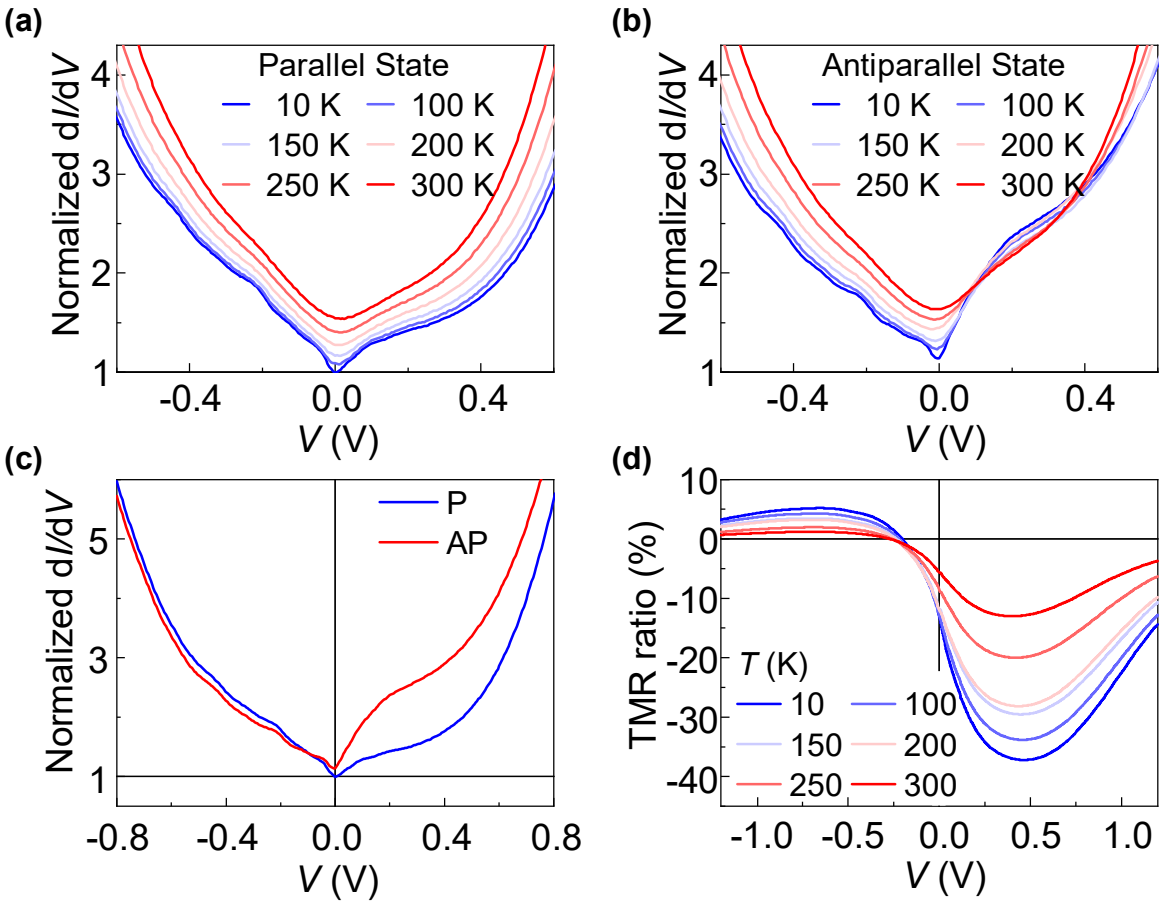

Figure 3: Bias dependence of the differential conductance dI/dV for Fe/MgAlO$_x$/Fe$_4$N MTJ. (a,b) Bias dependence of normalized dI/dV (divided by G_p(0V, 10K)) at different temperatures in (a) P and (b) AP states, respectively. (c) Bias dependence of normalized dI/dV for both states measured at 10 K. (d) Bias dependence of the TMR ratio at different temperatures deduced by the I-V measurements.

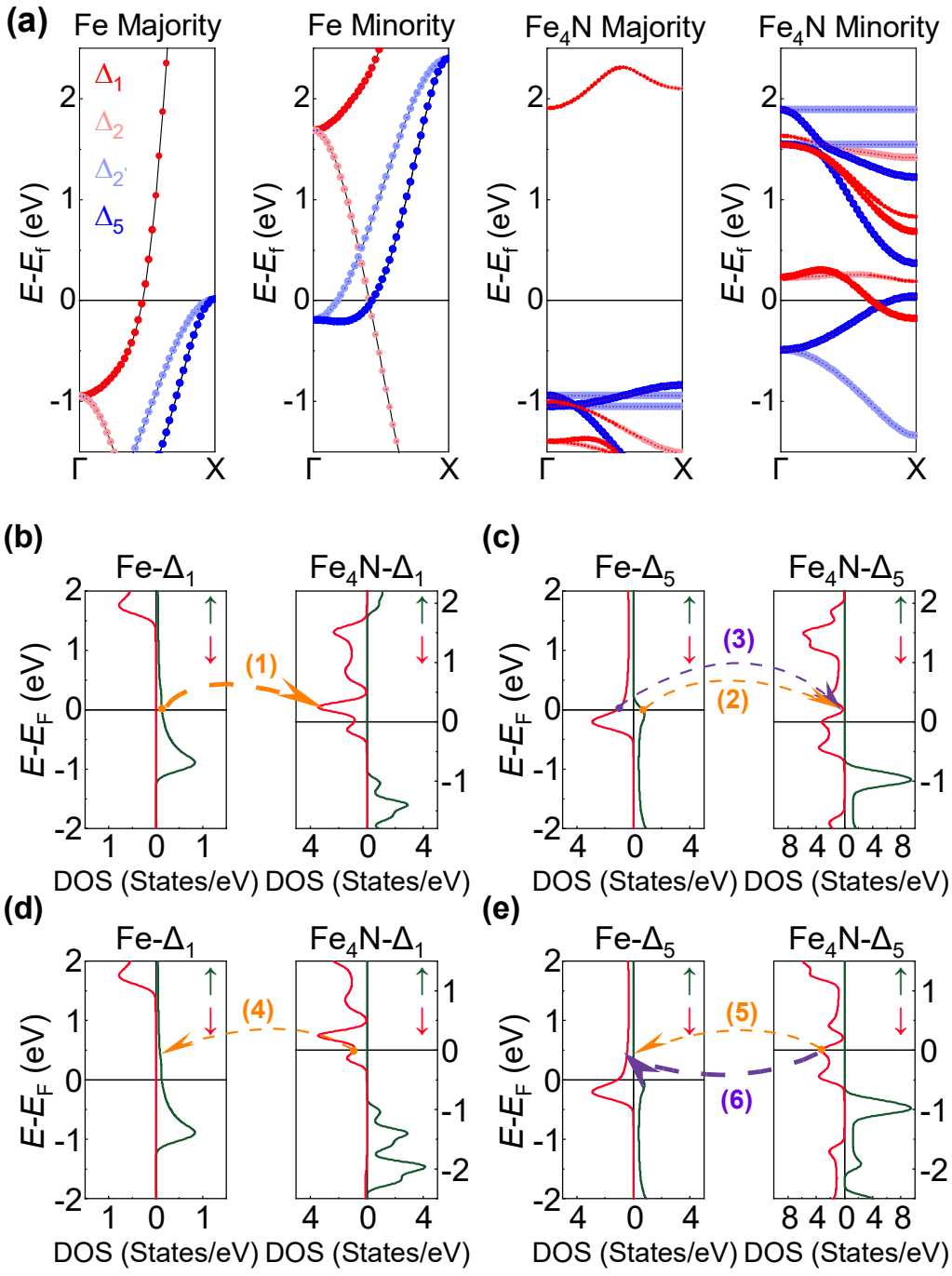

Figure 4: First principle calculations of band structures of bulk Fe and Fe_4N. (a) Symmetry and spin-resolved band structures of bulk Fe and Fe_4N along the transport direction (Γ-X). (b-e) Symmetry and spin-resolved DOS for $k_{//}$=0 of bulk Fe and Fe_4N as a function of the energy; (b,c) correspond to the tunneling under the positive bias, and (d,e) correspond to the tunneling under the negative bias. Dash lines represent the tunneling channels.

TOC figure:

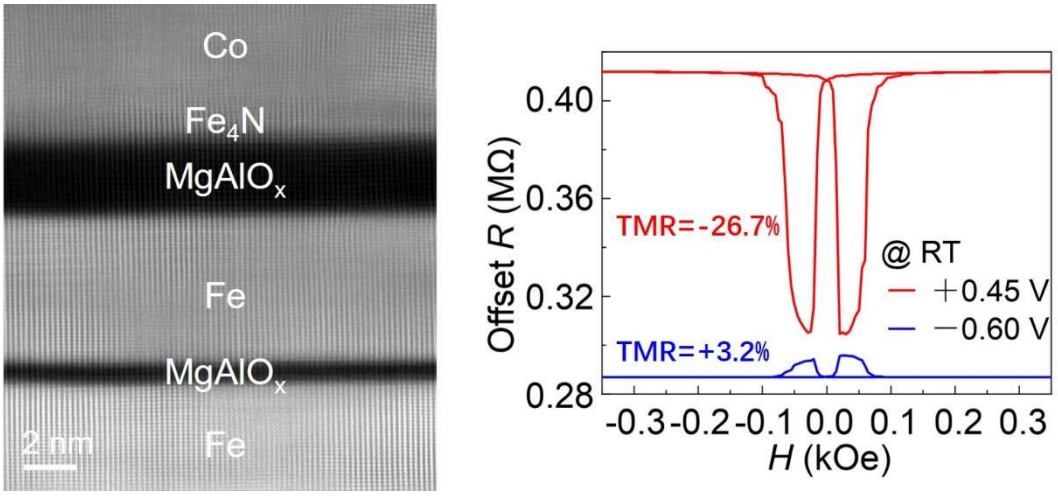
Co
Fe4N
MgAlOx
Fe
MgAlOx
2 nm
Fe
0.40
0.36
0.32
0.28
Offset R (MΩ)
TMR=-26.7%
TMR=+3.2%
@ RT
+0.45 V
−0.60 V
-0.3 -0.2 -0.1 0.0 0.1 0.2 0.3
H (kOe)